The Redshift Dependence of the Radio Flux of Gamma-Ray Bursts and Their Host Galaxies

Z. B. Zhang[1,2] , P. Chandra[3] , Y. F. Huang[4] , and D. Li[5,6]

[1] College of Physics and Engineering, Qufu Normal University, Qufu 273165, People's Republic of China; z-b-zhang@163.com
[2] Department of Physics, College of Physics, Guizhou University, Guiyang 550025, People's Republic of China
[3] National Centre for Radio Astrophysics, Tata Institute of Fundamental Research, P.O. Box 3, Pune 411007, India
[4] Department of Astronomy, Nanjing University, Nanjing 210023, People's Republic of China; hyf@nju.edu.cn
[5] National Astronomical Observatories of China, Chinese Academy of Sciences, 20A Datun Road, Beijing 100020, People's Republic of China
[6] CAS Key Laboratory of FAST, NAOC, Chinese Academy of Sciences, Beijing 100020, People's Republic of China

Abstract

Using multiwavelength observations of radio afterglows, we confirm the hypothesis that the flux density of gamma-ray bursts (GRBs) at a fixed observing frequency is invariable when the distance of the GRBs increases, which means the detection rate will be approximately independent of redshift. We study this behavior theoretically and find that it can be well explained by the standard forward shock model involving a thin shell expanding in either a homogeneous interstellar medium (ISM) or a wind environment. We also found that short GRBs and supernova-associated GRBs, which are at relatively smaller distances, marginally match the flux–redshift relationship and they could be outliers. We rule out the assumption that the medium density evolves with redshift as $n \propto (1 + z)^4$ from the current measurements of n and z for short and long GRBs. In addition, the possible dependence of host flux on the redshift is also investigated. We find that a similar redshift independence of the flux exists for host galaxies as well, which implies that the detection rate of radio hosts might also be independent of the redshift. It is also hinted that most radio hosts have spectral indices ranging from $\beta_h \simeq -1$ to 2.5 in statistics. Finally, we predict the detection rates of radio afterglows by next-generation radio telescopes such as the Five-hundred meter Aperture Spherical Telescope (FAST) and the Square Kilometer Array (SKA).

Key words: gamma-ray burst: general – hydrodynamics – methods: data analysis – radio continuum: general

1. Introduction

The radio afterglow of gamma-ray bursts (GRBs) was first discovered by Frail et al. (1997) for GRB 970508. Long-lasting radio afterglows are essentially immune to the geometry of the initial ejecta and thus can offer us an ideal way to estimate the true energy E_γ; this is because the radio afterglows are emitted at relatively later epochs when the Lorentz factor drops to sub-/ non-relativistic levels (Berger et al. 2004; Shivvers & Berger 2011; Wygoda et al. 2011; Mesler & Pihlström 2013). There are some additional advantages of radio observations, such as: (1) compared with X-ray and optical emissions, the radio afterglow lasts much longer that more detailed observations can be performed and can provide key clues to diagnose the intrinsic properties of the explosion, (2) radio observations can play an important role in revealing the structure of the surrounding medium and the geometry of the outflow (i.e., measuring the tiny angular size of afterglows via interstellar scintillation), as well as in revealing the progenitors of the explosions (e.g., Frail 2003), and (3) like many other astronomical objects such as compact stars, supernova (SN) remnants, interstellar medium, intergalactic medium, and radio lobes and jets of galaxies driven by central black holes, GRBs produce synchrotron radio emissions with a "steep" spectrum at later epochs, which indicates that their intensities increase strongly toward the low-frequency regime, thus they can be more conveniently observed in radio for a relatively long period. It is interesting to note that far-infrared observations show that the detection rate of GRB hosts is consistent with the idea that GRBs trace cosmic star formation rates (Kohn et al. 2015).

Ciardi & Loeb (2000) argued that the detectability of radio afterglows by ground-based radio telescopes is somewhat independent of redshifts. It is mainly based on theoretical studies showing that the dependence of the radio brightness on the redshift becomes increasingly weaker at higher redshifts (Ciardi & Loeb 2000; Gou et al. 2004). This argument has been proven by Karl G. Jansky Very Large Array (JVLA) observations and the Expanded Very Large Array Project (EVLA) at 8.5 GHz directly (Frail et al. 2006; Chandra & Frail 2012). In addition, Chandra & Frail (2012) showed that the detection rate starts to become independent of redshift after a redshift of 3. Such an effect makes it possible for us to observe very distant GRBs (up to $z > 15$) with large radio telescopes (e.g., Zhang et al. 2015). However, how the radio fluxes of GRB host galaxies evolve with their redshifts is still largely uncertain.

Observationally, roughly one-third of all GRBs with precise localization have been detected at radio frequencies (Chandra & Frail 2012; Chandra 2016). This rate is much lower than those at higher observing frequencies, where for instance 93% of GRBs observed in gamma-rays are also detected in X-ray bands and 75% are detected in optical bands. Furthermore, radio afterglows are more difficult to detect at lower radio frequencies owing to the self-absorption or influence of the host galaxies (e.g., Berger et al. 2001; Berger 2014; Li et al. 2015). Chandra & Frail (2012) presented a large radio afterglow sample of 304 GRBs, including 33 short-hard bursts, 19 X-ray flashes, and 26 GRB/SN candidates. Their sample also includes several low-luminosity bursts and high-redshift bursts, whose radio afterglows are even more difficult to detect due to their low energetics or large distances, and the interference

from the host galaxies. Recently, Li et al. (2015) proposed an interesting method to infer the contributions of the host galaxies at observational frequencies of $\nu \leqslant 10$ GHz. They found that at lower radio frequencies, the contribution of hosts becomes more important. An empirical relation was derived to approximate the frequency dependence of the host contribution, which can help to significantly increase the detectability of radio afterglows and should be particularly helpful in the upcoming era of large telescopes (Burlon et al. 2015; Zhang et al. 2015).

The properties of GRB host galaxies are important in understanding the nature of GRBs. For instance, one can use the hosts to study the large-scale environments, the burst energetics (once the redshift is determined from the optical spectrum of the host galaxy), and further constraints on the nature of GRB progenitors. Berger (2014) pointed out that different populations of short and long GRBs also differ significantly in their host galaxies (see also Zhang et al. 2009). Savaglio et al. (2009) used optical and near-IR (NIR) photometry and spectroscopy methods to study stellar masses, star formation rates, dust extinctions, and metallicities of a large set of GRB hosts. They found that GRBs can be used as a good probe to study star-forming galaxies. Their samples include 46 objects in the redshift interval $0 < z < 6.3$, with an average of $z \sim 1$. In their data set, about 90% of the hosts have relatively small redshifts of $z < 1.6$. Stanway et al. (2014) later reported their radio continuum observations of 17 GRB host galaxies with the Australia Telescope Compact Array (ATCA) and VLA at 5.5 and 9.0 GHz, respectively. Their samples span a redshift range of 0.5–1.4. Recently, Kohn et al. (2015) presented their analysis of the far-infrared properties of an "unbiased" set of GRB host galaxies. Their samples include 20 *BeppoSAX* and *Swift* GRBs, among which eight bursts are listed with known redshifts (the average value is $z = 3.1$). They constrained the dust masses and star formation rates (SFRs) of the hosts, and found that GRBs may trace the SFR of luminous galaxies in an unbiased way up to $z > 2$. The interesting result by Li et al. (2015), that the ratio of the host flux density to the peak flux of GRB afterglow is tightly correlated with the observing frequency, may also shed new light on the environment properties of GRBs. However, we notice that little is known about the spectra of GRB hosts in radio bands except for the special event of GRB 980703 (Berger et al. 2001), the host spectral index of which was estimated to be $\beta_h \approx -1/3$ from three data points at different frequencies. Observationally, most normal galaxies, such as M82 and our Milk Way Galaxy, usually have the spectral power-law index of $-3/4$ (Condon 1992; Carilli & Yun 1999). In principle, the synchrotron radiation mechanism may result in a positive spectrum index in the radio bands (e.g., Sari et al. 1998; Gao et al. 2013). The positive indices observed in a few GRBs thus indicate that they could have originated from some special types of galaxies, such as starburst or active galaxies.

In this study, we present a large data set of GRBs whose afterglows, as well as their hosts, are observed in radio wavelengths. The data are collected from the literature and are described in Section 2. In Section 3, using multiband observational data of GRB afterglows, we re-examine whether the radio fluxes are dependent on the redshifts and compare the results with theoretical predictions. We also examine how the radio fluxes of the hosts evolve with the redshifts from the data set. The detectability of GRBs by different large radio telescopes, such as the Square Kilometer Array (SKA; Dewdney et al. 2009) and the Five-hundred-meter Aperture Spherical radio Telescope (FAST; Nan et al. 2011; Li et al. 2013) are studied. Finally, we present our conclusions and brief discussion in Section 4.

2. Data Collection

For the purpose of studying the redshift dependence of the flux of radio afterglows, 17, 30, and 54 GRBs available in Chandra & Frail (2012) at the three frequencies of $\nu = 1.43$, 4.86, and 8.46 GHz, respectively, were used. Their peak radio fluxes, peak times, and redshifts were all measured. We will use these observational data in our current study. Note that two short GRBs (050724 and 051221) and three SN-associated GRBs (980425, 031203 and 060218) are included in these samples. Although the numbers of these special GRBs are too limited, they might still be helpful in giving us hints on the systematic differences between them and normal long GRBs.

In general, the radio hosts of GRBs are so faint that only about three hosts could be detected each year by all current ground-based radio telescopes. However, it is interesting to investigate the redshift dependence of the flux of GRB host galaxies in radio bands and compare it with that of afterglows. For this target, we have also collected 37 long bursts with 47 measured host flux densities at several low/medium frequencies of 1.43, 3.0, 4.9, 5.5, 9.0, 37.5, and 222 GHz. The sample selection criteria are as follows: (1) the radio afterglow of the corresponding GRB was observed, (2) the redshift was measured, and (3) the host flux densities have been reported in the literature. The data and their references are listed in Table 1. In this table, Columns (1)–(8) correspond to the burst names, durations (T_{90}), cosmological redshifts, isotropic γ-ray energies, observing frequencies, host flux densities (F_{host}), references for F_{host}, and telescopes, respectively.

In Table 1, the first set of entries ($N = 16$; from line 1 to line 24) represents relatively bright events with 24 measurements, with the peak of the radio afterglow being clearly observed as well. For these events, we are assured that the host fluxes have been relatively accurately measured and the interference from their afterglows has been subtracted. Hereafter, we call this subsample the "Gold-Host Sample." The second data set ($N = 18$; from line 25 to line 46) in Table 1 denotes those 18 hosts with 22 measurements without peak fluxes of radio afterglows observed. In Table 1, there are 11 and 16 host measurements collected from Perley et al. (2015) and Stanway et al. (2014), respectively, and around one-third of the GRBs are associated with SNe.

As demonstrated in previous works, GRB 100418A is an ultralong burst without an SN association (e.g., Jia et al. 2012; Niino et al. 2012). Its radio flux densities reached $363 \pm 48\ \mu$Jy and $199 \pm 57\ \mu$Jy at 5.5 and 9.0 GHz, respectively. The unusually high radio flux densities are believed to be from the radio afterglows instead of the host galaxies (Stanway et al. 2014). In addition, two high-redshift GRBs (050904 and 090323) are not included in Table 1. The peak fluxes of radio afterglows at 8.46 GHz are measured for these three GRBs, but the host fluxes at our frequencies of interest are not directly available. For example, the host galaxy of GRB 090423 was not detected at higher frequencies of $\nu_{\mathrm{obs}} = 222$ and 37.5 GHz by the Atacama Large Millimeter Array (ALMA) and the ATCA, but the upper limits of the host flux at these frequencies have been constrained by Berger et al. (2014) and Stanway et al. (2011).

Table 1
Observed Parameters of Radio Host Galaxies of GRBs

GRB	T_{90} (s)	z	$E_{\gamma,\mathrm{iso}}$ (10^{51} erg)	ν_{obs} (GHz)	F_{host} (μJy)	Ref.	Telescope
(1)	(2)	(3)	(4)	(5)	(6)	(7)	(8)
980425[a]	31	0.0085	0.002	4.8	420 ± 50[b]	1	ATCA
				8.64	<180	1	ATCA
980703	90	0.966	69	1.43	68 ± 6.6[b]	2	VLA
				4.86	42.1 ± 8.6[b]	2	VLA
				8.46	39.3 ± 4.9[b]	2	VLA
000210	10	0.85	200	8.46	18 ± 9	4	VLA
000301C	10	2.034	43.7	8.46	18 ± 7[b]	3	VLA
000418	30	1.119	75.1	1.43	59 ± 15[b]	3	VLA
				4.86	41 ± 13[b]	4	VLA
				8.46	41 ± 12[b]	4	VLA
000926	25	2.039	270	8.46	23 ± 9[b]	3	VLA
010222	170	1.477	133	4.86	23 ± 8[b]	3	VLA
011121[a]	105	0.362	45.5	4.86	<120	12	VLA
020405[a]	40	0.69	110	8.46	<42	9	VLA
031203[a]	30	0.105	0.115	1.39	254 ± 46[b]	10	ATCA
				2.37	191 ± 37[b]	10	ATCA
				5.5	216 ± 50[b]	11	ATCA
050525A[a]	9	0.606	20.4	5.5	<15.6	5	ATCA
050824[a]	23	0.83	1.5	5.5	42.3 ± 33.2	5	ATCA
051022	200	0.809	630	5.5	<23.0	5	ATCA
060218[a]	128	0.033	0.003	3.0	5.52 ± 3.88	8	VLA
090423[c]	10.3	8.23	110	37.5	<9.3	6	ATCA
				222	<33	7	ALMA
090424	50	0.544	44.7	5.5	36.6 ± 28	5	ATCA
050223	22.5	0.592	0.87	5.5	90.5 ± 30.1[b]	5	ATCA
				9.0	93 ± 48	5	VLA
050922C	4.5	2.198	37.4	3.0	8.8 ± 3.5[b]	8	VLA
051006	34.8	1.059	35.8	3.0	9.08 ± 3.17[b]	8	VLA
060729[a]	115.3	0.54	13.8	5.5	65.4 ± 27.8	5	ATCA
				9.0	60 ± 41	5	VLA
060814	145.3	1.92	307	3.0	11.34 ± 3.1[b]	8	VLA
				5.5	43.6 ± 23.5	5	ATCA
060908	19.3	1.884	44	3.0	<4.53	8	VLA
060912A	5	0.937	17.3	3.0	4.54 ± 3.37	8	VLA
061110A	40.7	0.758	13.2	3.0	14.2 ± 6.08	8	VLA
061121	81.3	1.314	272	3.0	17.07 ± 5.47[b]	8	VLA
070129	461	2.34	26.9	3.0	<4.92	8	VLA
070306	210	1.497	88	3.0	11.31 ± 2.84[b]	8	VLA
070506	4.3	2.31	4.23	3.0	<3.69	8	VLA
070508	20.9	0.82	70	5.5	35.0 ± 28.2	5	ATCA
071112C	15	0.823	5.3	5.5	50.1 ± 25.2	5	ATCA
080413B	8	1.1	16.5	5.5	7.6 ± 4.7	5	ATCA
080710	120	0.845	49.5	5.5	42.6 ± 28.8	5	ATCA
081007[a]	10	0.529	0.16	5.5	38.1 ± 26.7	5	ATCA
100621A	63.6	0.542	43.5	5.5	120 ± 32[b]	5	ATCA
				9.0	106 ± 42[b]	5	VLA

Notes. References are given for the host radio flux density: 1. Michałowski et al. (2009), 2. Berger et al. (2001), 3. Perley & Perley (2013), 4. Berger et al. (2003a), 5. Stanway et al. (2014), 6. Stanway et al. (2011), 7. Berger et al. (2014), 8. Perley et al. (2015), 9. Berger et al. (2003b), 10. Michałowski et al. (2012), 11. Stanway et al. (2010), 12. Frail et al. (2003)
[a] SN-associated GRBs.
[b] Host flux densities that are larger than the 3σ level.
[c] High-redshift GRBs.

3. Results

In this section, we will first study the redshift dependence of the radio flux densities of GRB afterglows and hosts based on our samples. Then we use the newly found redshift dependence of the flux to constrain the spectral parameters of these host galaxies. Finally, we investigate the detectability of GRB radio afterglows by next-generation radio instruments, such as the Low-Frequency Array or LOFAR (van Haarlem et al. 2013), FAST (Nan et al. 2011; Li et al. 2013), and SKA (Dewdney et al. 2009), etc. In the following theoretical calculations, we take typical values for the key parameters of the forward shock model. For example, the microphysical parameters of electrons and magnetic fields are $\varepsilon_e = 0.1$ and $\varepsilon_B = 0.01$ (e.g., Panaitescu & Kumar 2002;
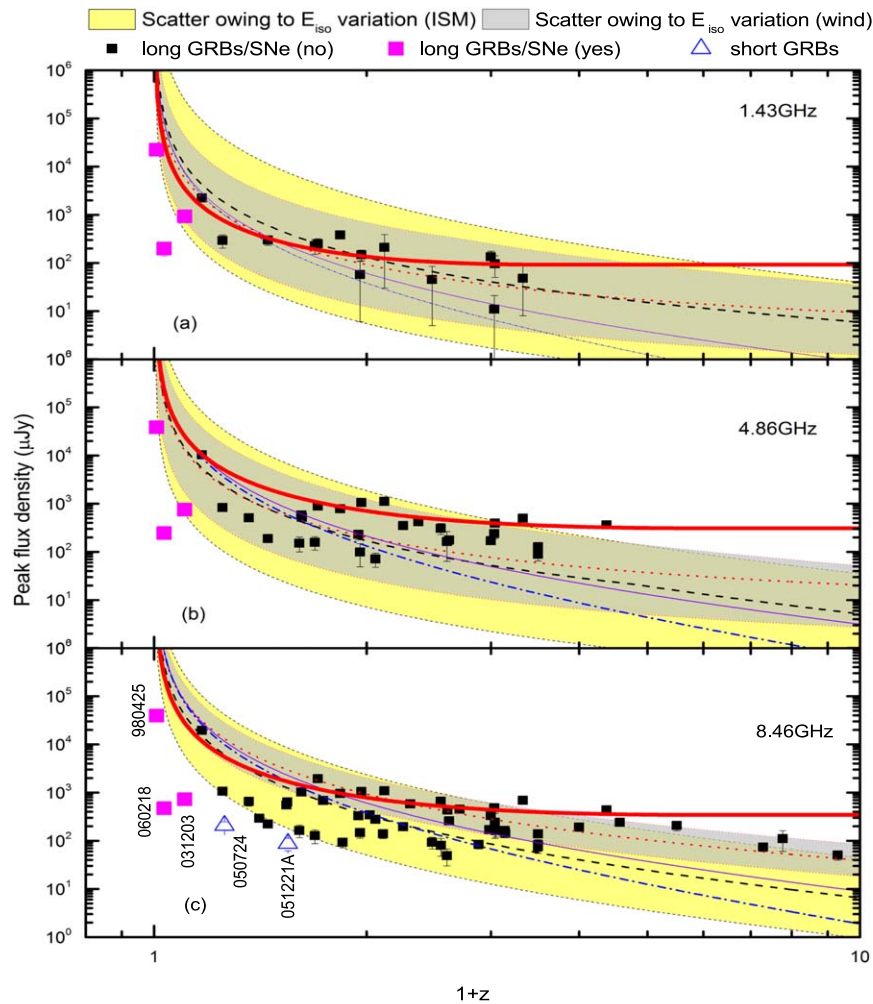
Figure 1. Peak flux density vs. redshift for GRB radio afterglows, with the effects of the parameter E_{iso} specifically illustrated. Panels (a)–(c) correspond to GRBs at the observing frequencies of 1.43 GHz, 4.86 GHz, and 8.46 GHz, respectively. The symbols are marked on the legend. The dashed–dotted line plots the flux density, which is evolving according to the inverse square of the luminosity distance. The solid line is the flux density scaling with an additional negative K-correction effect (see text). The light yellow and gray regions represent the redshift dependencies of the flux in the ISM and wind cases, respectively, for an average isotropic energy of $E_{iso} = 2 \times 10^{52}$ erg and with one order of magnitude scatter. The thick solid line represents the fourth power-law relation of $n = n_0(1 + z)^4$ with $n_0 = 0.1$ cm^{-3}.

Zhang et al. 2003), respectively. The average isotropic energy of our radio-selected sample with peak flux measurements from Chandra & Frail (2012) is about $E_{iso} = 2 \times 10^{52}$ erg, thus this value will be used in our numerical calculations below. Finally, the power-law index of electron distribution is assumed to be $p = 2.3$.

3.1. Redshift Dependence of the Flux for GRB Afterglows

The peak flux densities of radio afterglows at $\nu = 1.43, 4.86$, and 8.46 GHz are plotted against the redshifts in Figures 1–5. It is clearly seen that the radio flux density does exhibit a weak dependence on the redshift. Generally speaking, the peak flux densities are weaker for more distant events. In fact, such a weak dependence has been noticed in several previous studies (e.g., Ciardi & Loeb 2000; Gou et al. 2004; Frail et al. 2006; Chandra & Frail 2012). Below, we give a quantitative explanation for the dependence in the framework of the standard forward shock model.

3.1.1. Methodology

Systematic analytical solutions for GRB afterglows involving forward shock emission in either the fast cooling regime or the slow cooling regime have been addressed by many authors (e.g., Mészáros & Rees 1997; Sari et al. 1998; Chevalier & Li 1999; Huang et al. 1999, 2000; Zhang & Mészáros 2004; Wu et al. 2005; Zhang et al. 2006; Gao et al. 2013). Following usual treatments, we assume that the ambient density at radius R is $n = AR^{-k}$ cm^{-3}, where k is a constant index characterizing the density form of the medium and R is the radius of a blast wave in units of centimeter. There are mainly two kinds of density forms. In the homogeneous interstellar medium (ISM) case, the density is a constant, and we have $k = 0$. In the stellar wind case, the density decreases outward so that we have $k = 2$. In the latter case, we can further write the density as $n = AR^{-2}$ cm^{-3}, where $A = 3 \times 10^{35}A_*$ cm^{-1} (a typical wind parameter of $A_* = 0.2$ will be taken in our calculations; see below). We assume $n_0 = 0.1$ cm^{-3} and $A_* \simeq 0.2$ to be the best parameters for the ISM and wind cases, respectively. Wu et al. (2005) argued that the parameter A_* should be quite small to fit typical observational data. In fact, the deduced values of A_* for a few long GRBs span four orders of magnitude, ranging from 5×10^{-4} to 3.5, with the median value being 0.18 (Panaitescu & Kumar 2002, 2003; Price et al. 2002; Dai & Wu 2003; Chevalier et al. 2004). Therefore, our wind parameter of $A_* \simeq 0.2$ is a reasonable value. However, we should bear in mind that although we have taken a typical set
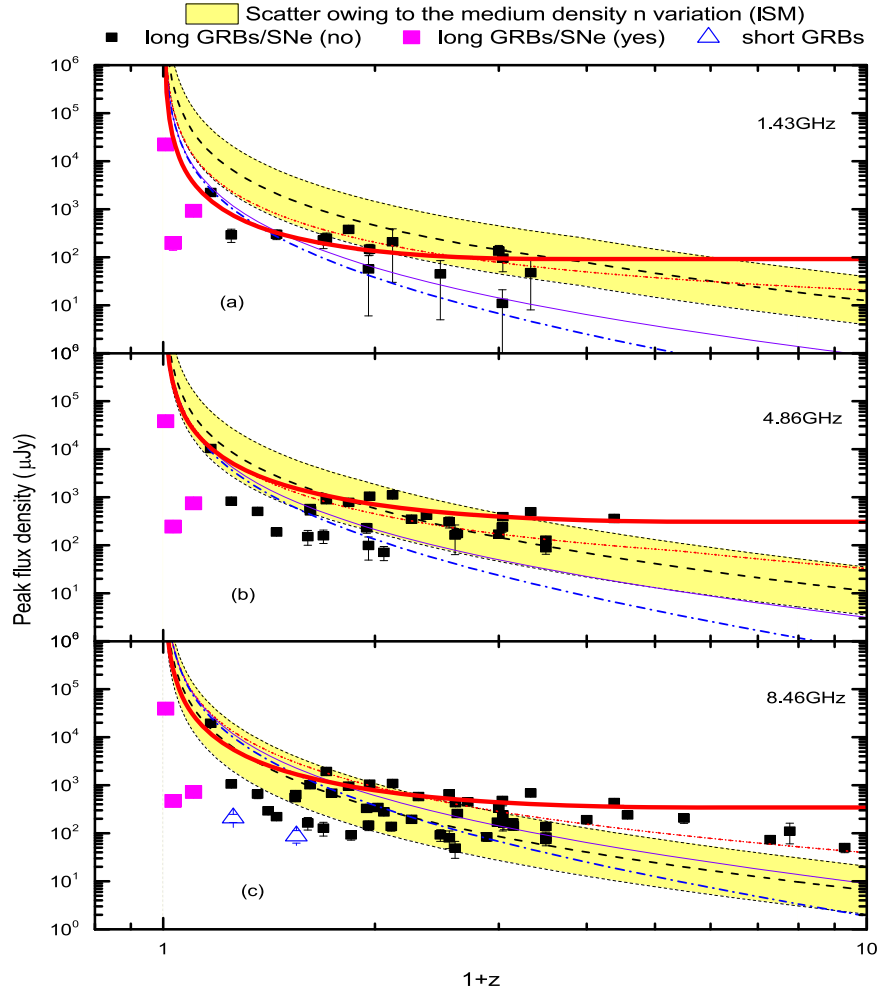
Figure 2. Peak flux density vs. redshift of GRB radio afterglows, with the effects of the parameter n specifically illustrated. The light yellow regions represent the redshift dependencies of the flux in the homogeneous ISM case, for an average interstellar medium density of $n = 0.1$ cm^{-3} and with one order of magnitude scatter. All other symbols are the same as in Figure 1.

of parameters to calculate the afterglow light curves, these parameters actually could differ from burst to burst, thus the actual afterglow light curves should also vary accordingly. In Figures 1–5, we have also varied several microphysical parameters to illustrate their effects. Finally, we assume that the outflows are adiabatic in our calculations, since radio afterglows are usually observed at relatively late stages. It is consistent with the fact that the radiation efficiency ε is negligible after the blast wave enters the self-similar deceleration phase.

After considering three characteristic frequencies (i.e., ν_c: the cooling frequency; ν_m: the typical synchrotron frequency; ν_a: the self-absorption frequency), the observed flux density at a certain frequency ν can be given by

$$
F_\nu = F_{\nu,\max} \times \begin{cases} (\nu/\nu_a)^2 (\nu_a/\nu_m)^{1/3}, & \nu < \nu_a; \\ (\nu/\nu_m)^{1/3}, & \nu_a < \nu < \nu_m; \\ (\nu/\nu_m)^{-(p-1)/2}, & \nu_m < \nu < \nu_c; \\ (\nu/\nu_c)^{-p/2}(\nu_c/\nu_m)^{-(p-1)/2}, & \nu_c < \nu, \end{cases} \quad (1)
$$

when $\nu_a < \nu_m < \nu_c$ (Case I) or by

$$
F_\nu = F_{\nu,\max} \times \begin{cases} (\nu_m/\nu_a)^{(p+4)/2}(\nu/\nu_m)^2, & \nu < \nu_m; \\ (\nu_a/\nu_m)^{-(p-1)/2}(\nu/\nu_a)^{5/2}, & \nu_m < \nu < \nu_a; \\ (\nu/\nu_m)^{-(p-1)/2}, & \nu_a < \nu < \nu_c; \\ (\nu/\nu_c)^{-p/2}(\nu_c/\nu_m)^{-(p-1)/2}, & \nu_c < \nu, \end{cases} \quad (2)
$$

when $\nu_m < \nu_a < \nu_c$ (Case II) in the slow cooling regime during the late afterglow stage. Here, the quantity $F_{\nu,\max}$ denotes the flux density at the characteristic frequency of ν_m. The majority of electrons are emitting electromagnetic waves at around this frequency. The observed flux density can peak at either ν_m or ν_a in the above two cases, and thus can be calculated as

$$
F_{\nu,t_p}(z) = F_{\nu,\max} \begin{cases} 1, & (\nu_a < \nu_m < \nu_c); \\ (\nu_m/\nu_a)^{(p-1)/2}, & (\nu_m < \nu_a < \nu_c), \end{cases} \quad (3)
$$

where $t_p \, (\equiv t_{p,\mathrm{obs}})$ represents the observed peak time of the radio afterglow. We caution that in each case, the peak flux density will evolve into the same form as $F_{\nu,t_p}(z) = F_{\nu,\max}$ eventually. In practice, there are even three other possible $\nu_a > \nu_c$ cases, each requiring quite different electron distributions (Gao et al. 2013). Those cases occur only in very rare scenarios and are ignored in this study.

Our recent investigations show that the radio afterglows at lower frequencies of a few GHz usually peak at dozens of days after the bursts (Zhang et al. 2015). These peaks often occur during the Phase 3 defined in Gao et al. (2013). If the sideways expansion effect of the jet is negligible, one can easily get the dependence of the peak flux density on the redshift at any given frequency. In the ISM case ($k = 0$), with a constant density of n_0,
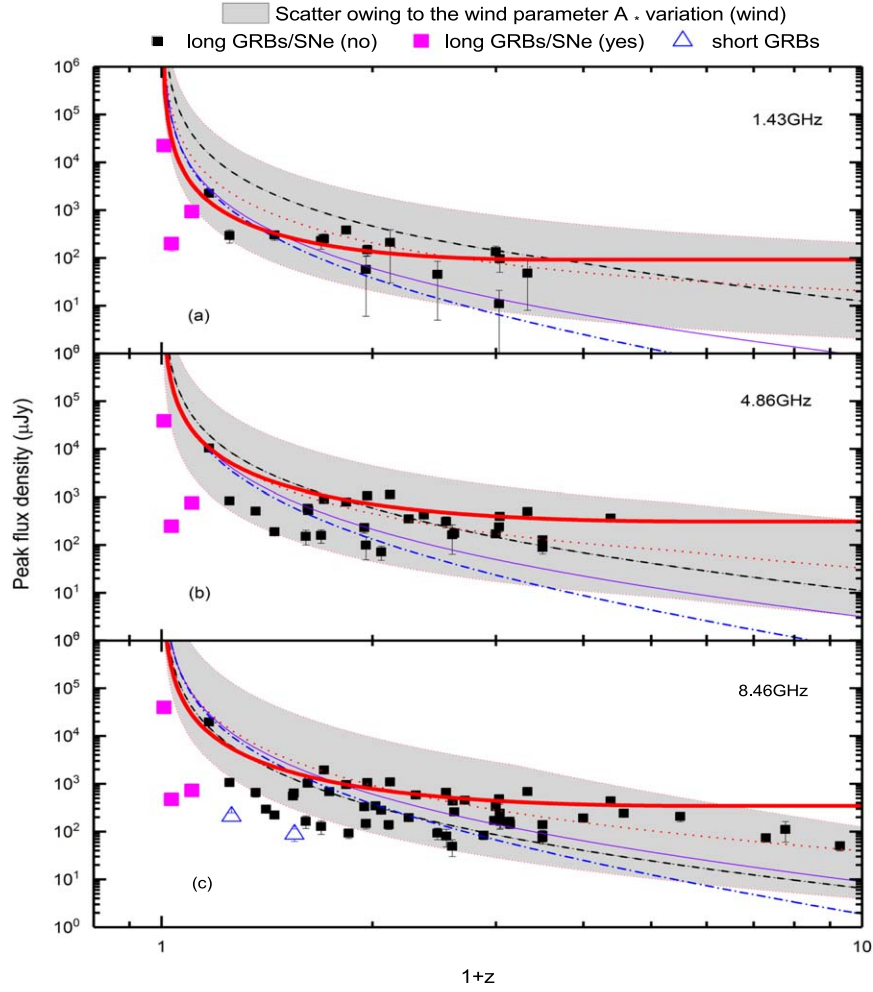
Figure 3. Peak flux density vs. redshift of GRB radio afterglows, with the effects of the parameter A_* specifically illustrated. The light gray regions represent the redshift dependencies of the flux in the wind medium case for an average wind parameter of $A_* = 0.2$ and with one order of magnitude scatter. All other symbols are the same as in Figure 1.

we have $\nu_m \propto (1+z)^{1/2}$, $\nu_c \propto (1+z)^{-1/2}$, and $F_{\nu,\mathrm{max}} \propto (1+z)D_l^{-2}(z)$. In the wind medium case ($k=2$), we get $\nu_m \propto (1+z)^{1/2}$, $\nu_c \propto (1+z)^{-3/2}$, and $F_{\nu,\mathrm{max}} \propto (1+z)^{3/2}D_l^{-2}(z)$. Here, $D_l(z)$ denotes the luminosity distance given by $D_l(z) = \frac{(1+z)c}{H_0}\int_0^z \frac{dz'}{E(z')}$, where $E(z') = \frac{H(z')}{H_0} = [\Omega_m(1+z')^3 + \Omega_k(1+z')^2 + \Omega_\Lambda f(z')]^{1/2}$, with $\Omega_\Lambda = 0.68$, $\Omega_m = 0.32$, $\Omega_k = 0$, and $H_0 \simeq 67\,\mathrm{km\,s^{-1}\,Mpc^{-1}}$ according to the latest cosmology observations (Planck Collaboration et al. 2014), and $f(z) = exp[3\int_0^z \frac{1+w(z')}{1+z'}dz'] \equiv 1$ as $w(z) \simeq -1$ for a flat ΛCDM cosmological model.

According to Equation (3), in the late slow cooling phase ($\nu_a < \nu_m < \nu_c$), the redshift dependence of the flux can be characterized by

$$F_{\nu,t_p}(z) \propto (1+z)D_l^{-2}(z) \qquad (4)$$

for the ISM medium, or

$$F_{\nu,t_p}(z) \propto (1+z)^{3/2}D_l^{-2}(z) \qquad (5)$$

in the stellar wind case. It is noticeable that both Equations (4) and (5) are independent of ν_a. Instead, if the condition of $\nu_m < \nu_a < \nu_c$ is satisfied for the other slow cooling case in Equation (3), the redshift dependence of the peak flux can be characterized by

$$F_{\nu,t_p}(z) \propto (1+z)^{\frac{7p+3}{2(p+4)}}D_l^{-2}(z) \qquad (6)$$

as $\nu_a \propto (1+z)^{(p-6)/[2(p+4)]}$ for the ISM medium, or

$$F_{\nu,t_p}(z) \propto (1+z)^{\frac{6p+9}{2(p+4)}}D_l^{-2}(z) \qquad (7)$$

as $\nu_a \propto (1+z)^{(p-2)/[2(p+4)]}$ in the wind case.

Note that all of the above flux–redshift relations have been obtained on condition that the medium density is independent of the cosmological redshift. In the constant-density ISM case, if the medium has a redshift dependence such as $n = n_0(1+z)^4$ (Ciardi & Loeb 2000), then we can obtain $\nu_m \propto (1+z)^{1/2}$, $\nu_c \propto (1+z)^{-9/2}$, and $F_{\nu,\mathrm{max}} \propto (1+z)^3 D_l^{-2}(z)$. In this case, our Equations (4) and (6) will change to

$$F_{\nu,t_p}(z) \propto (1+z)^3 D_l^{-2}(z) \qquad (8)$$

as $\nu_a \propto (1+z)^{7/5}$ for $\nu_a < \nu_m < \nu_c$, and

$$F_{\nu,t_p}(z) \propto (1+z)^{\frac{3p+27}{2(p+4)}}D_l^{-2}(z) \qquad (9)$$

as $\nu_a \propto (1+z)^{(p+10)/[2(p+4)]}$ for $\nu_m < \nu_a < \nu_c$. The peak radio luminosity can be determined from $L_{\nu,t_p}(z) = 4\pi D_l^2(z)F_{\nu,t_p}(z)(1+z)^{-1}$ without K-correction, or $L_{\nu,t_p}(z) = 4\pi D_l^2(z)F_{\nu,t_p}(z)(1+z)^{-1}k$ with a K-correction factor of
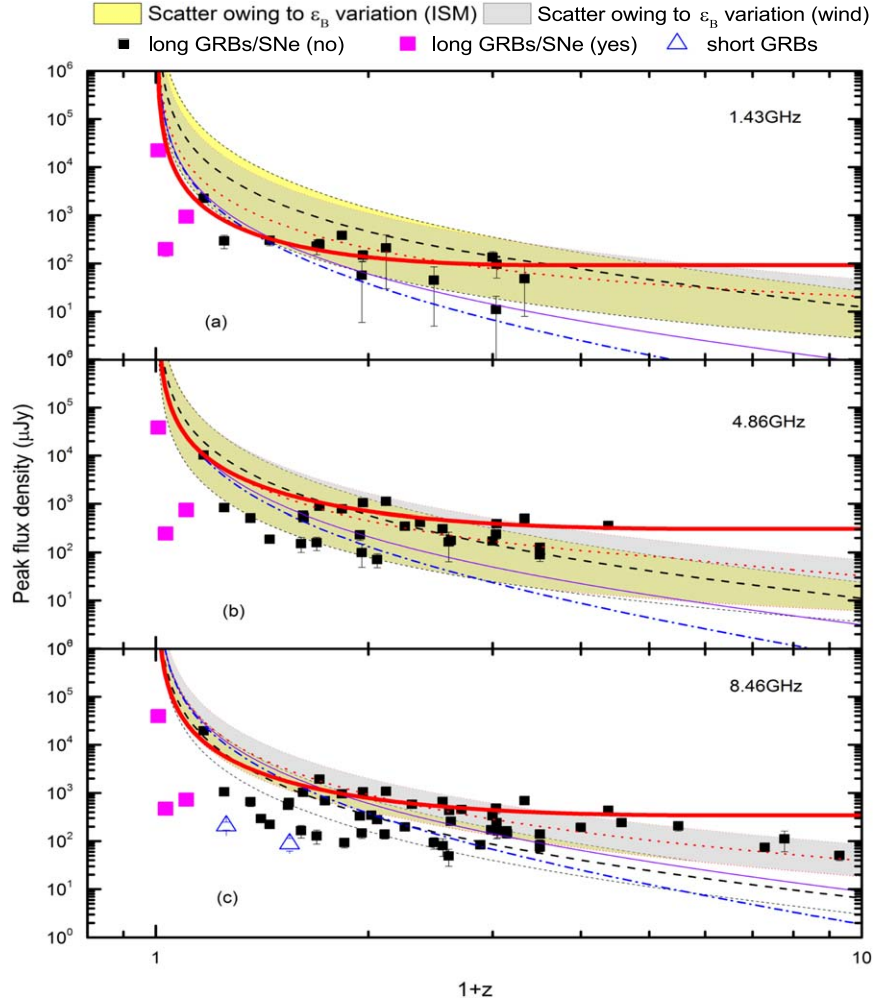
Figure 4. Peak flux density vs. redshift of GRB radio afterglows, with the effects of the parameter ε_B specifically illustrated. The light yellow and gray regions represent the redshift dependencies of the flux in the ISM and wind medium cases, respectively, for an average magnetic field of $\varepsilon_B = 0.01$ and with one order of magnitude scatter. All other symbols are the same as in Figure 1.

$k = (1 + z)^{\alpha - \beta}$, where $\alpha \sim 0$ and $\beta \sim 1/3$ are the normal temporal and spectral indices defined in $F_\nu(t) \propto t^\alpha \nu^\beta$ (Soderberg et al. 2004; Frail et al. 2006; Chandra & Frail 2012).

3.1.2. Model Testing

Taking the above medium parameters ($E_{\rm iso}$, n_0, A_1, ε_e, and ε_B) but allowing them to vary within an order of magnitude separately, we have calculated the evolution profiles of the peak flux density versus redshift. The results are shown in Figures 1–5. From Figure 1 we see that at high-frequency bands, the radio afterglows can still be largely observable at high redshifts. On the contrary, short and SN-associated GRBs are more likely detected mainly in the nearby universe. Additionally, we stress that both the ISM and the wind environment models can account for the redshift dependence of the flux. The power-law index τ in the relation $F_{\nu,t_p} \propto (1 + z)^\tau D_l^{-2}(z)$ from Equations (4)–(9) has been compared for the three different medium cases in Table 2. Interestingly, we find that the peak fluxes drop sharply in the ISM case (which has a constant density at all redshifts), but decrease slowly in the ISM case of $n \propto (1 + z)^4$. In view of the currently available observational results in Figures 1–5, we emphasize that the latter fourth power-law case can be excluded empirically.

This point can be further examined below when we vary the other four parameters (n_0, A_*, ε_B, and ε_e) individually for one order of magnitude to investigate the dependence of the peak flux density on the redshift. It proves that the four parameters can independently influence the evolution of the flux with redshift in the sense shown from Figures 2–5. However, it is hard to judge from Figures 1–5 which interstellar medium model is better in statistics. Note that the redshift dependence of the peak flux is affected not only by the structure of the circumburst medium (ISM or wind), but also by the different microphysical parameters, such as $E_{\rm iso}$, n, A_*, ε_e, and ε_B. For a given medium structure, the variations of the microphysical parameters may influence the peak-flux–redshift relationship. Interestingly, our theoretical investigations on the flux–redshift relation may give the upper limit for the electron equipartition parameter as $\varepsilon_e \leqslant 0.1$. It is less than the usually assumed value of $1/3$ for fast cooling electrons at early times (see Wu et al. 2005).

Gou et al. (2004) have theoretically studied how the medium density changes with redshift in the framework of the forward and reverse shock models. They found that there is no correlation between n and z. Now we examine this issue from the observational viewpoint. We use the medium's density data derived for a number of GRBs by Chandra & Frail (2012) and
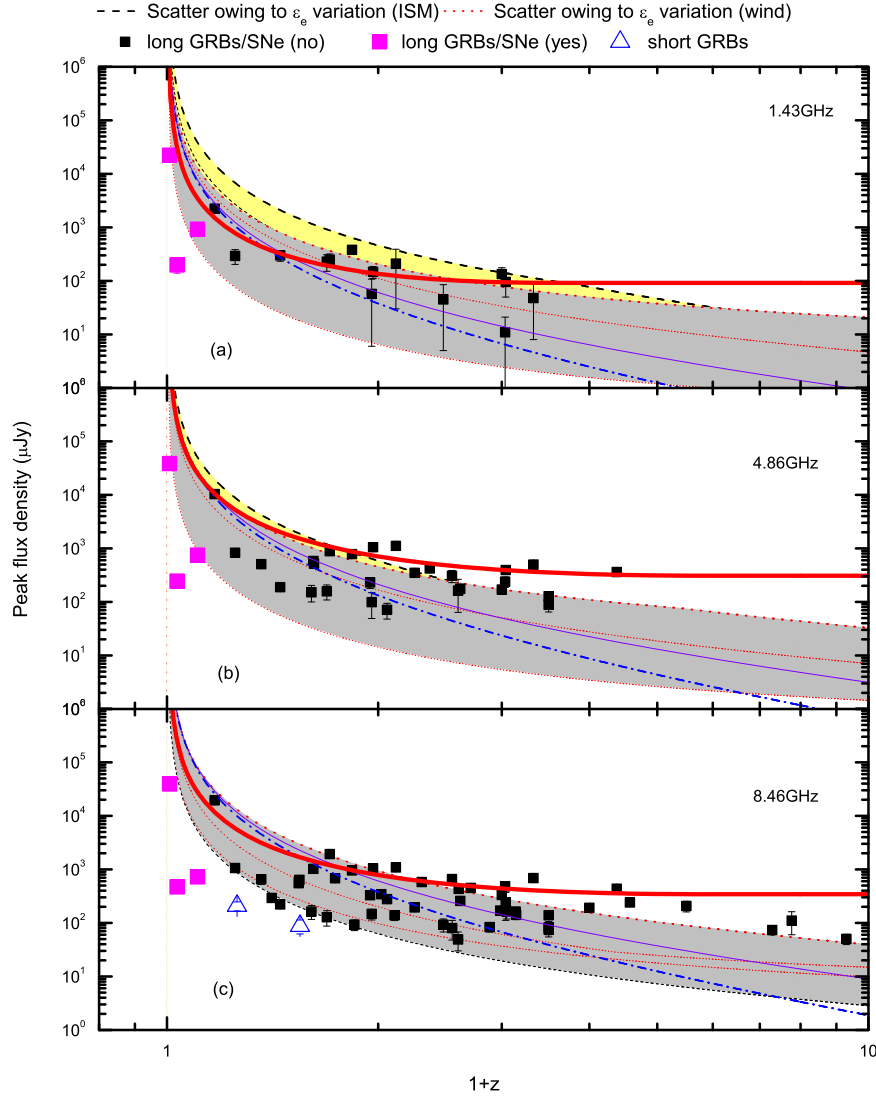
Figure 5. Peak flux density vs. redshift of GRB radio afterglows, with the effects of the parameter ε_e specifically illustrated. The light yellow and gray regions represent the redshift dependencies of the flux in the ISM and wind medium cases, respectively, for an average electron parameter of $\varepsilon_e = 0.1$ and with one order of magnitude scatter. All other symbols are the same as in Figure 1.

Table 2
Power-law Index τ of the Peak-flux–Redshift Relation

Medium	Density Form	τ in Case I	τ in case II
ISM	$n = 1 \, \mathrm{cm}^{-3}$	1	$(7p + 3)/[2(p + 4)] \simeq 1.5$
ISM	$n = (1 + z)^4 \, \mathrm{cm}^{-3}$	3	$(3p + 27)/[2(p + 4)] \simeq 2.7$
wind	$n = 3 \times 10^{35} A_* R^{-2} \, \mathrm{cm}^{-3}$	3/2	$(6p + 9)/[2(p + 4)] \simeq 1.8$

Note. For further details, the other parameters involved (n, A_*, R, and p) can be found in Section 3. Note that $F_{\nu, t_p} \propto (1 + z)^\tau D_l^{-2}(z)$ has been defined in the main text.

Fong et al. (2015). In particular, Fong et al. (2015) presented the medium densities for 38 short GRBs and found that most of these GRBs occurred in a lower density medium ($n < 1 \, \mathrm{cm}^{-3}$). In Figure 6, we plot the number density versus the redshift for these events, which include 4 short and 24 long GRBs that have both redshift measurements and density estimation. This figure generally shows that the derived medium density does *not* evolve with the redshift. In Figure 6, we specifically examined the power-law relation of $n = n_0(1 + z)^4$. We take

$n_0 = 0.1$, 1, and $10 \, \mathrm{cm}^{-3}$, and plot the curves respectively. We see that the observational data points do not follow these curves. Figure 6 thus clearly confirms that the number density and redshift are not correlated with each other.

Note that the observed peak time for radio afterglows may suffer from cosmological time dilation. It is interesting to examine whether this effect exists in the observational data. Figure 7 shows the peak time versus cosmological redshift for 10 GRBs with measured radio fluxes of both afterglows and
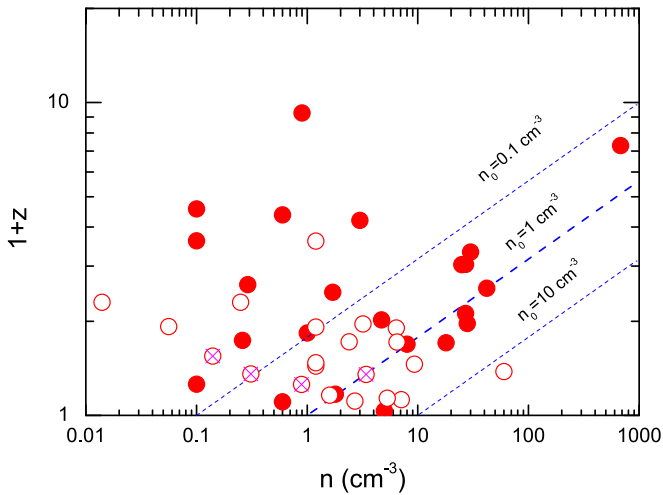
Figure 6. Theoretically derived medium density vs. redshift for a number of GRBs. The data are mainly taken from Chandra & Frail (2012) and Fong et al. (2015). The solid and empty circles represent 24 long and 21 short GRBs, respectively. The four crossed circles stand for short bursts with radio afterglows detected so far. The dashed lines show the different density forms of $n = n_0(1 + z)^4$ with $n_0 = 10$, 1, and 0.1 cm^{-3}, respectively.

hosts from Table 1. The peak times of these GRBs were derived by Chandra & Frail (2012). In panel (a), it can be clearly seen that the observed peak time does have a tight correlation with the redshift. The best fitted relation is $t_{p,obs} \propto (1 + z)$, with a correlation coefficient of $r \simeq 0.85$, which corresponds to a 99% confidence level (not including GRB 100418A). In panel (b), after correcting for the cosmological time dilation effect, we see that the intrinsic peak time is largely independent of the redshift, and it tends to be a constant of about 5 days especially at high redshifts. In both panels, GRB 100418A especially stands out as an obvious outlier. In fact, GRB 100418A is a unique long burst without an SN association (Niino et al. 2012). In addition to the very late peak time of radio emission, it also has an unusual long-lasting X-ray and optical afterglow, with an especially long optical plateau (Marshall et al. 2011). It has been suggested that this GRB is powered by the continuous activity of the central engine (Moin et al. 2013; Li et al. 2015).

3.2. Redshift Dependence of the Flux for the Host Galaxies

We now use 36 GRB hosts (except the upper limits) listed in Table 1 to study how the host flux $F_{\nu,h}$ evolves with redshift. The results are plotted in Figure 8. For this purpose, a power-law form of $F_{\nu,h} \propto \nu^{\beta_h}$ has been assumed for the GRB hosts. As discussed in Section 3.1, the spectral luminosity of host galaxies would similarly satisfy $L_{\nu,h}(z) = 4\pi D_l^2(z) F_{\nu,h}(z)(1 + z)^{-1-\beta_h}$, which gives $F_{\nu,h}(z) = [L_{\nu,h}(z)/4\pi D_l^2(z)](1 + z)^{1+\beta_h}$. If the GRB hosts can also be regarded as a standard candle, which means their $L_{\nu,h}(z)$ concentrate in a relatively narrow range, one can then derive the correlation between the host flux and the redshift. In fact, the radio spectral luminosities of GRB host galaxies do concentrate at around $\overline{L_{\nu,h}(z)} \simeq 3.6 \times 10^{29}$ erg s^{-1} Hz^{-1}, as shown in the right panel of Figure 9. Optimistically, from Figure 8, we find that the GRB hosts exhibit weak redshift dependence of the flux when the distance of the GRBs becomes increasingly farther. It is also found that the spectral index β_h of hosts generally varies between -1 and 2.5, when the three low-redshift SN-associated bursts (980425, 031203, and 060218,

which seem to be obvious outliers in Figure 8) are not included. It does not conflict with previous results on β_h, such as the $\beta_h = -0.75$ reported by Condon (1992). The advantage of our method is that it can be used to constrain the spectral index of β_h roughly when the spectrum of the host is available but for the limited observation data points. A high index of $\beta_h \simeq 2$ (2.5) indicates that the radio emission of GRB hosts may be affected by synchrotron self-absorption, similar to that of GRB afterglows in the slow cooling phase (e.g., Mészáros & Rees 1993; Paczynski & Rhoads 1993; Katz & Piran 1997). Alternatively, the value of β_h can also be explained by the synchrotron radiation itself as shown in Equations (1)–(2), where the host spectra peaks at ν_m (ν_a) and β_h is equal to 2 (2.5) if $\nu_a < \nu_m$ ($\nu_m < \nu_a$) is satisfied. It is noticeable that the majority of the fainter hosts in Figure 8 are reported by Perley et al. (2015). Unfortunately, only half of the GRBs associated with these faint radio hosts were detected with radio afterglows. What makes things even worse is that the peak flux measurements are unavailable for almost all of them, except for GRB 060218. This is consistent with the fact that the radio hosts are on average at least one order of magnitude weaker than the peak brightness of the radio afterglow. The median flux densities at 3 and 8.5 GHz in Table 1 (excluding those upper limits) are about 9.1 ± 3.2 and 23 ± 9 μJy, respectively.

In Figure 9, we investigate the correlation between the radio luminosity of GRB hosts and redshift. The average spectral luminosity of the 36 well-detected GRB host galaxies in Table 1 is $\sim 3.6 \times 10^{29}$ erg s^{-1} Hz^{-1}, with a standard deviation of $\sigma_{\log L_{\nu,h}} \simeq 0.94$. When the three SN-associated GRBs, 980425, 031203, and 060218, are excluded, we can get the mean spectral luminosity as $\sim 0.95 \times 10^{30}$ erg s^{-1} Hz^{-1}. To compare with the detection limit of FAST and SKA, we use Equation (9) of Zhang et al. (2015) to calculate the 5σ level sensitivities of these instruments at a representative frequency of 1.43 GHz. A factor of $1/(1 + z)$ for the cosmological time dilation effect has been considered in the calculations. Identifying GRB host fluxes at very high redshifts is a huge challenge at lower frequencies. Even at higher frequency, as of 2015 August, only one upper limit of the host flux density had been obtained for high-redshift bursts (i.e., GRB 090423), at $\nu = 222$ GHz by ALMA (Berger et al. 2014) and at $\nu = 37.5$ GHz by ATCA (Stanway et al. 2011). We notice that the host luminosity of GRB 980425 is about three orders of magnitude dimmer than the average host spectral luminosity of $\sim 3.6 \times 10^{29}$ erg s^{-1} Hz^{-1} of all the measured host flux densities, although it is already the brightest radio host among these samples. It is worth pointing out that at least about 92% of these radio hosts can be obtained by FAST and SKA successfully.

3.3. Detection Rates

As usual, one can calculate the GRB rates by assuming that GRBs and the star formation rate (SFR) are closely related so that GRBs trace the SFR exactly. Here we follow Yüksel et al. (2008) to predict the detection rates of GRBs by current and future large radio instruments such as several upcoming SKA pathfinders, FAST, Australian Square Kilometer Array Path-finder (ASKAP), MeerKAT, etc. The number of GRBs detectable in the redshift range of $z = 0$–4 (Yüksel et al. 2008) can be given by
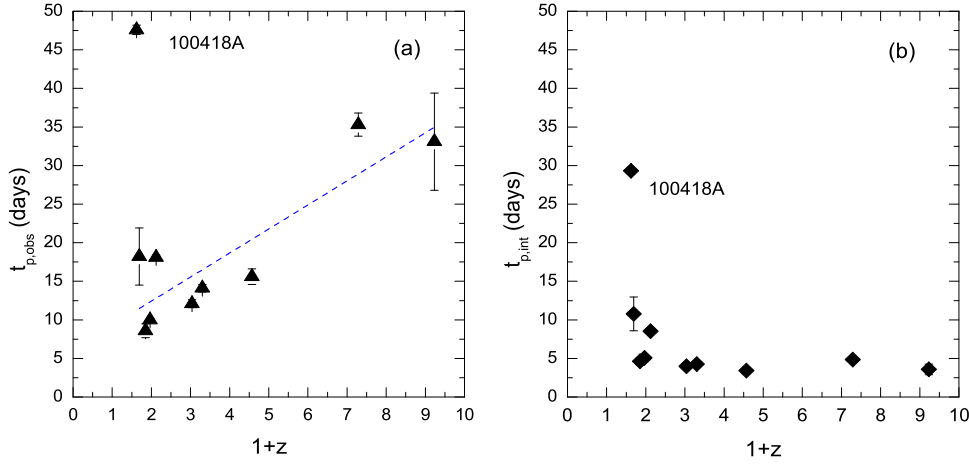
Figure 7. Correlation between the redshift and the peak time of the 8.5 GHz radio afterglows. In panel (a), the *Y*-axis is simply the observed peak time, while in panel (b), the *Y*-axis is the intrinsic peak time (i.e., corrected for the cosmological time dilation effect). Note that GRB 100418A seems to be an outlier in these plots; the reason why is still quite uncertain. The best linear fit to the nine bursts, except for GRB 100418A, is shown by the dashed line in panel (a).
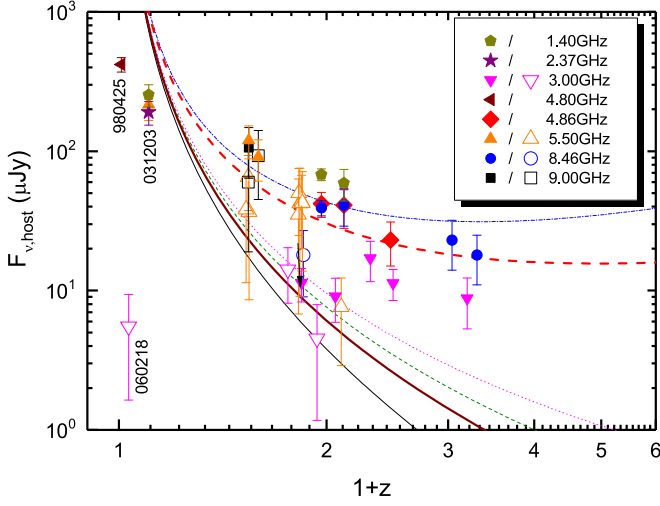

Figure 8. Host radio flux vs. redshift at multiple frequencies for the observational data in Table 1 (not including the upper limits). The thin solid line corresponds to the simple inverse square law of the luminosity distance without *K*-correction ($\beta_h = -1$); The remaining lines represent different scenarios for *K*-corrections (thick solid line: $\beta_h = -1/3$, Berger et al. 2001; dashed: $\beta_h = 0$; dotted: $\beta_h = 1/3$; red thick dashed: $\beta_h = 2$; dashed–dotted: $\beta_h = 2.5$). Observational data points at different frequencies are denoted by different solid/empty symbols for values larger/smaller than 3σ confidence levels, correspondingly.

$$\mathcal{N}_{0\to 4}^{\mathrm{obs}} = \Delta t \frac{\Delta\Omega}{4\pi} \int_0^4 dz F(z)\varepsilon(z)\dot{\rho}_*(z)\frac{dV(z)/dz}{1+z}, \quad (10)$$

where Δt and $\Delta\Omega$ are the total live time and the angular sky coverage of the telescope, respectively; $F(z) \equiv F_0$ and $\varepsilon(z) = \varepsilon_0(1+z)^\zeta$ have been defined with two unknown constants (F_0 and ε_0) and $\zeta \simeq 1.5$ has been used by Kistler et al. (2008); $1/(1+z)$ is the correction factor due to cosmological time dilation; $dV(z)/dz = 4\pi (c/H_0)D_c^2(z)/\sqrt{(1+z)^3\Omega_m + \Omega_\lambda}$ represents the comoving volume per unit redshift where the comoving distance $D_c(z)$ is related to the luminosity distance $D_l(z)$ via $D_l(z) = (1+z)D_c(z)$; $\dot{\rho}_*(z)$ is the star formation rate function, which is usually assumed to be (Hopkins & Beacom 2006)

$$\dot{\rho}_*(z) = \dot{\rho}_0\left[(1+z)^{a\eta} + \left(\frac{1+z}{B}\right)^{b\eta} + \left(\frac{1+z}{C}\right)^{c\eta}\right]^{1/\eta}, \quad (11)$$

with $a = 3.4$, $b = -0.3$, $c = -3.5$, $\dot{\rho}_0 = 0.02\,M_\odot\,\mathrm{yr}^{-1}\,\mathrm{Mpc}^{-3}$, $\eta \simeq -10$, $B \simeq 5000$, and $C \simeq 9$ (Yüksel et al. 2008). Then, the comoving event rate of GRBs can be calculated from $\dot{n}_{\mathrm{GRB}}(z) = \varepsilon(z)\dot{\rho}_*(z)$.

Using Equation (10), we can estimate the all-sky number of detectable GRBs up to a certain redshift z as

$$\mathcal{N}_{0\to z}^{\mathrm{obs}} = \mathcal{N}_{0\to 4}^{\mathrm{obs}} \times \frac{\Delta\Omega_1\Delta t_1}{\Delta\Omega\Delta t}\frac{\int_0^z dz(1+z)^{\alpha-1}\dot{\rho}_*(z)dV(z)/dz}{\int_0^4 dz(1+z)^{\alpha-1}\dot{\rho}_*(z)dV(z)/dz},$$

(12)

where Δt_1 and $\Delta\Omega_1$ stand for the total observation time and the angular sky coverage of the telescope. The observed GRB number is mainly determined by the observation time, the field of view (FoV), and the sensitivity. Specifically, for a GRB to be detected, the observed flux density should be above the instrumental flux threshold given by $F_{\mathrm{th},\nu} = (1 + z_{\max})L_\nu[4\pi D_l^2(z_{\max})]^{-1}$ (*K*-correction not included here), where L_ν is the spectral luminosity at the observing frequency ν and $z_{\max}$ is the maximum observable redshift for the burst. Note that the detection rate will slightly decrease if the *K*-correction effect is taken into account. In Figure 10, we plot the peak spectral luminosity–redshift distribution for the observed radio afterglows. The redshifts of these GRBs generally range from $z = 0$ to 4. From this plot, we obtain the mean peak luminosity of radio afterglows as $4^{+12}_{-1} \times 10^{30}\,\mathrm{erg\,s^{-1}\,Hz^{-1}}$.

We have applied Equation (12) to calculate the detection rate of radio afterglows versus the threshold flux at 10 typical frequencies. The results are illustrated in Figure 11. We find that FAST is more powerful than most other existing or upcoming instruments, except for SKA (see Table 3). For example, FAST has a theoretical sensitivity of $2\,\mu\mathrm{Jy}$ at $\nu = 1.4\,\mathrm{GHz}$ for an integration time of 1 hr, which is much better than the other two SKA pathfinders, i.e., MeerKAT with $30\,\mu\mathrm{Jy}$ and ASKAP with $60\,\mu\mathrm{Jy}$ (it is also noticeable that the
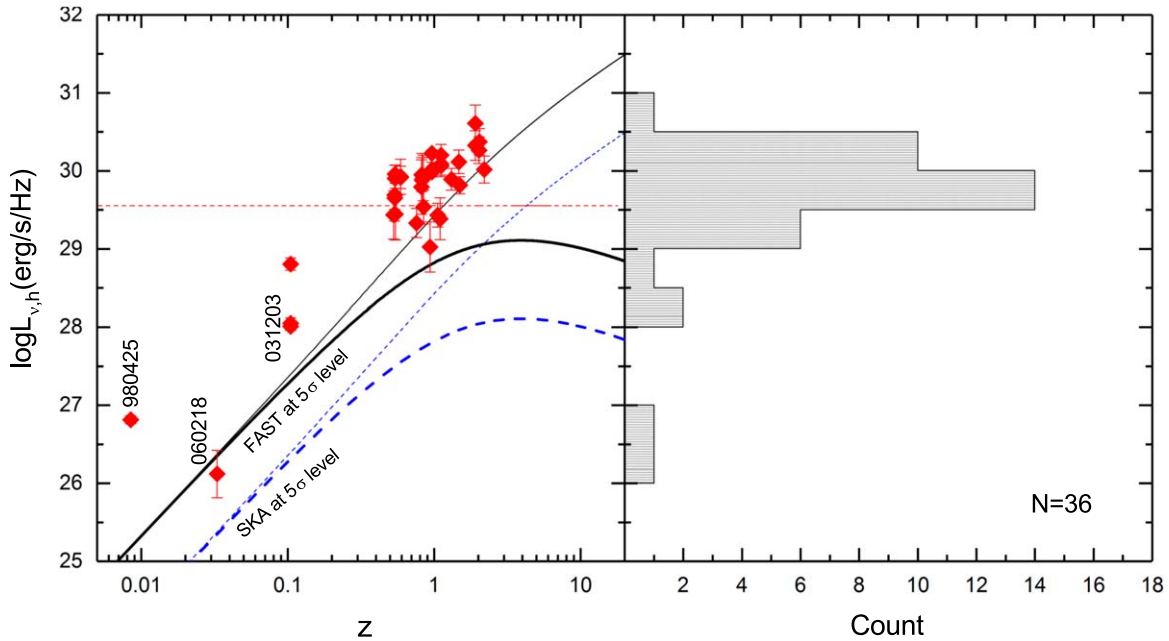
Figure 9. Radio spectral luminosity vs. redshift (left panel) and luminosity histogram of 36 host flux densities (right panel). The sensitivities of FAST and SKA with (thick curves) and without (thin curves) *K*-correction are given for $\nu = 1.43$ GHz at the 5σ level by assuming a 1 hr integration time.
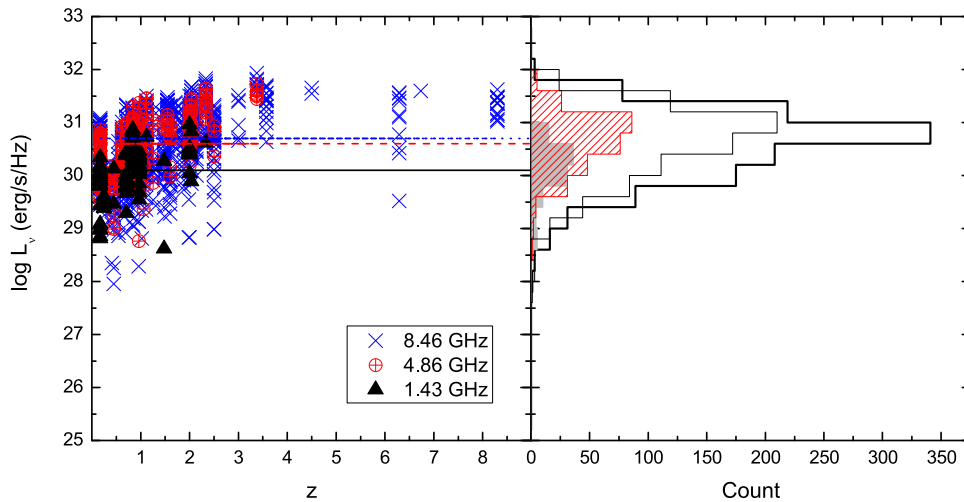

Figure 10. Left panel: peak luminosities vs. redshifts for GRB radio afterglows, with 101, 279, and 784 measurements at 1.43 GHz, 4.86 GHz, and 8.46 GHz, respectively. The corresponding average spectral luminosities are denoted by three horizontal lines, which are in the range of 1×10^{30}–5×10^{30} erg s^{-1} Hz^{-1}. Right panel: radio luminosity distributions for the 1.43 GHz (shade), 4.86 GHz (hatched), 8.46 GHz (thin line), and the entire (thick line) samples.

upgraded Giant Meterwave Radio Telescope (uGMRT), as one of pathfinders of the SKA, works in 1420-150 MHz bands with a few hundred MHz bandwidth and can reach sensitivity up to 10–20 μJy in various bands within a few hours of integration). It is capable of detecting ~270 GRB radio afterglows per square degree per year at $\nu = 1.4$ GHz. The detection rate is thus higher than VLA by about one order of magnitude. SKA is expected to acquire an even better sensitivity of 0.5 μJy in reality, and it will then generate an even higher detection rate of 464 deg^{-2} yr^{-1} at the same frequency. But it should also be noted that we have ignored two observational effects in our calculations, i.e., the "confusion" effect and the "baseline drift" effect. These effects generally would cause the wide band (i.e., continuum) observations at frequency $\nu < 5$ GHz to be much more difficult for a single-dish radio telescope (Condon 2002). First, the confusion noise will not go down even if we increase

the integration time. Thanks to the broader FoV, huge single dishes can image relatively large areas and smooth those low-brightness sources to complement interferometric observations. In other words, interferometers including the JVLA may run rings around Arecibo-like single dishes for GRB continuum studies unless the above primary problems are successfully solved technically (see also Chandra 2016; Chandra et al. 2016). The second serious problem for the single dish will be baseline drifts caused by small receiver gain fluctuations and by changing spillover as the galaxy is tracked. These baseline drifts can be mitigated by various scanning and beam-switching schemes, but they are very inefficient and will occupy a lot of telescope time (D. A. Frail 2015, private communication). In addition, all kinds of radio frequency interferences (RFI) around may also have a non-negligible effect on the single-dish receivers. These deeply motivate us to consider how to overcome these similar puzzles

Table 3
Key Parameters of Current and Future Radio Telescopes

Telescope	Frequency (MHz)	Bandpass (MHz)	ν_{obs} (MHz)	A_{eff}/T_{sys} (m^2/K)	Ω_{FoV} [a] (deg^2)	F_{lim} (μJy)	Detection Rate ($\#/deg^2\ yr^{-1}$)	Ref.
VLA	75–43000	1000	1430	100–200	0.22	50	11	1
		4000	4860		0.02	20	311	
		4000	8460		0.01	13	1703	
FAST	70–3000	70	100	2000	0.4	71	0.1	2
		140	200		0.1	26	2.2	
		280	400		0.025			
		460	800		0.006			
		570	1450		0.002	2	270	
		1000	2500		0.001			
LOFAR	10–80	3.66	60	400	74.99			3
	110–240	3.66	150	400	11.35	38	1	
ASKAP	700–1800	300	1400	>85	30	60	7.2	4
MeerKAT	500–2000	1500	1400	>160	1.1	30	21	5
MWA	80–300	30.72	150	7	610			6
SKA	50–20000	230	150	5000–10000	200	1	156	7
		9700	700		1–200	0.5	464	
		10000	5500		1			

Note. References: 1. Thompson et al. (1980); 2. Nan et al. (2011); 3. van Haarlem et al. (2013); 4. Johnston et al. (2008); 5. Booth et al. (2009); 6. Tingay et al. (2013); 7. Dewdney et al. (2009).
[a] The sky coverage is given by $\Omega = \pi(FoV/2)^2$, where the FoV of a given telescope or array can be estimated with $FoV = 1.22 \times \frac{\lambda}{D}$, in which λ is the observing wavelength and D is the effective aperture or the maximum length of the baseline between each dish pairs. For VLA, the FoV is determined using $FoV = \frac{45}{\nu_{(GHz)}}$ arcmin. For FAST, we have $FoV = \frac{14}{\nu_{(GHz)}}$ arcmin at different frequencies with a constant $D = 300$ m for the beam. All others are taken from the above references directly.
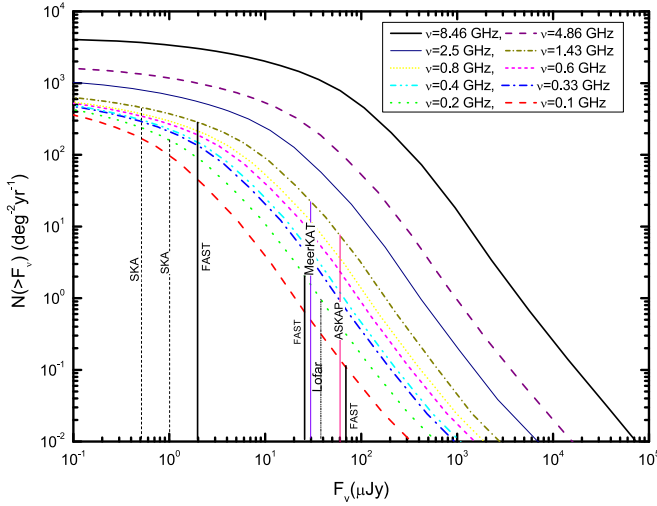

Figure 11. Cumulative flux distributions of radio afterglows at various observational frequencies. The vertical lines indicate the detection limits of different instruments, including LOFAR, ASKAP, FAST, MeerKAT, and SKA. The detecting sensitivities are calculated by assuming $\Delta \tau = 1$ hr, $\Delta \nu = 100$ MHz, and S/N = 5. Note that the vertical lines in this figure only refer to the sensitivity of the instrument at the frequency located at the top of the line.

for FAST. Hopefully, our results can shed new light on the studies of radio afterglows and hosts with the next-generation large telescopes, but need more technical developments to solve the above problems for the single-dish observations.

4. Conclusions

Based on the currently available radio data set, we analyze the statistical properties of GRB afterglows and hosts, paying special attention to the redshift dependence of the flux of both afterglows and hosts. We have also investigated the detectability of GRB afterglows and host galaxies at very high redshifts by different large radio telescopes. Our results are summarized as follows.

1. We verify the prediction that the observability of GRBs is largely independent of redshifts. Theoretically, we show that this feature is expected in the standard forward shock model for a thin shell expanding in either an ISM and/or a wind environment. When comparing with the observational data points, however, it is hard to distinguish which medium model is better since many of the microphysical parameters could vary at a certain range. Particularly, the fourth power-law relation of $n \propto (1 + z)^4$ is ruled out based on current observations, which is consistent with the previous work of Gou et al. (2004).

2. Using our samples of radio hosts, we have investigated the dependence of the host flux density on the cosmological redshift. A trend where the radio host flux becomes less dependent on the redshift at farther distances is found, which implies that the detectability of radio hosts may also be largely unrelated with redshift. Assuming a power-law spectrum of $F_{\nu,h} \propto \nu^{\beta_h}$ for inspecting the corresponding flux–redshift relation, we have used the observed host flux densities to constrain the spectral index of β_h ranging from -1 to 2.5 for most host galaxies. This may impose strong

constraints on the GRB physics and galaxy evolution theories. However, the radio spectral index of GRB host galaxies is only deduced from a limited number of events and needs to be confirmed by more samples in the era of larger telescopes.

3. Finally, we have explored the detection rates of GRB afterglows by different large radio telescopes such as FAST, LOFAR, MeerKAT, ASKAP, and SKA. FAST has an outstanding potential for very high-redshift radio afterglows. Therefore, we stress that if FAST as a single-dish telescope can overcome the so-called "confusion and baseline drift" difficulties for continuum observations at lower frequency of $\nu < 5$ GHz, it would be able to detect a large number of radio afterglows and thus play an important role in detecting these faint radio sources in the near future. Optimistically, FAST is expected to be better than other SKA pathfinders at higher frequency, say $\nu > 3$ GHz, hopefully in its second phase.

ORCID iDs

Z. B. Zhang ⓘ https://orcid.org/0000-0003-4859-682X
P. Chandra ⓘ https://orcid.org/0000-0002-0844-6563
Y. F. Huang ⓘ https://orcid.org/0000-0001-7199-2906
D. Li ⓘ https://orcid.org/0000-0003-3010-7661

References

Berger, E. 2014, ARA&A, 52, 43
Berger, E., Cowie, L. L., Kulkarni, S. R., et al. 2003a, ApJ, 588, 99
Berger, E., Kulkarni, S. R., & Frail, D. A. 2001, ApJ, 560, 652
Berger, E., Kulkarni, S. R., & Frail, D. A. 2004, ApJ, 612, 966
Berger, E., Soderberg, A. M., Frail, D. A., & Kulkarni, S. R. 2003b, ApJL, 587, L5
Berger, E., Zauderer, B. A., Chary, R.-R., et al. 2014, ApJ, 796, 96
Booth, R. S., de Blok, W. J. G., Jonas, J. L., et al. 2009, arXiv:0910.2935
Burlon, D., Ghirlanda, G., van der Horst, A., et al. 2015, arXiv:1501.04629
Carilli, C. L., & Yun, M. S. 1999, ApJL, 513, L13
Chandra, P. 2016, AdAst, 2016, 296781
Chandra, P., Anupama, G. C., Arun, K. G., et al. 2016, JApA, 37, 30
Chandra, P., & Frail, D. A. 2012, ApJ, 746, 156
Chevalier, R. A., & Li, Z. Y. 1999, ApJL, 520, L29
Chevalier, R. A., Li, Z. Y., & Fransson, C. 2004, ApJ, 606, 369
Ciardi, B., & Loeb, A. 2000, ApJ, 540, 687
Condon, J. J. 1992, ARA&A, 30, 575
Condon, J. J. 2002, ASPC, 278, 155
Dai, Z. G., & Wu, X. F. 2003, ApJL, 591, L21
Dewdney, P. E., Hall, P. J., Schilizzi, R. T., & Lazio, T. J. L. W. 2009, IEEEP, 97, 1482
Fong, W. F., Berger, E., Margutti, R., et al. 2015, ApJ, 815, 102
Frail, D. A. 2003, arXiv:astro-ph/0309557
Frail, D. A., Cameron, P. B., Kasliwal, M., et al. 2006, ApJL, 646, L99
Frail, D. A., Kulkarni, S. R., Berger, E., & Wieringa, M. H. 2003, AJ, 125, 2299
Frail, D. A., Kulkarni, S. R., & Nicastro, L. 1997, Natur, 389, 261
Gao, H., Lei, W. H., Zou, Y. C., et al. 2013, NewAR, 57, 141
Gou, L. J., Mészáros, P., Abel, T., & Zhang, B. 2004, ApJ, 604, 508
Hopkins, A. M., & Beacom, J. F. 2006, ApJ, 651, 142
Huang, Y. F., Dai, Z. G., & Lu, T. 1999, MNRAS, 309, 513
Huang, Y. F., Gou, L. J., Dai, Z. G., & Lu, T. 2000, ApJ, 543, 90
Jia, L.-W., Wu, X. F., Lü, H. J., et al. 2012, RAA, 12, 411
Johnston, S., Taylor, R., Bailes, M., et al. 2008, ExA, 22, 151
Katz, J. I., & Piran, T. 1997, ApJ, 490, 772
Kistler, M. D., Yüksel, H., Beacom, J. F., & Stanek, K. Z. 2008, ApJL, 673, L119
Kohn, S. A., Michalowski, M. J., Bourne, N., et al. 2015, MNRAS, 448, 1494
Li, D., Nan, R. D., & Pan, Z. C. 2013, IAUS, 291, 325, arXiv:1210.5785
Li, L. B., Zhang, Z. B., Huang, Y. F., et al. 2015, MNRAS, 451, 1815
Marshall, F. E., Antonelli, L. A., Burrows, D. N., et al. 2011, ApJ, 727, 132
Mesler, R. A., & Pihlström, Y. M. 2013, ApJ, 774, 77
Mészáros, P., & Rees, M. J. 1993, ApJL, 418, L59
Mészáros, P., & Rees, M. J. 1997, ApJ, 476, 232
Michałowski, M. J., Hjorth, J., Malesani, D., et al. 2009, ApJ, 693, 347
Michałowski, M. J., Kamble, A., Hjorth, J., et al. 2012, ApJ, 755, 85
Moin, A., Chandra, P., Miller-Jones, J. C. A., et al. 2013, ApJ, 779, 105
Nan, R. D., Li, D., Jin, C. J., et al. 2011, IJMPD, 20, 989
Niino, Y., Hashimoto, T., Aoki, K., et al. 2012, PASJ, 64, 115
Paczynski, B., & Rhoads, J. E. 1993, ApJL, 418, L5
Panaitescu, A., & Kumar, P. 2002, ApJ, 571, 779
Panaitescu, A., & Kumar, P. 2003, MNRAS, 346, 905
Perley, D. A., & Perley, R. A. 2013, ApJ, 778, 172
Perley, D. A., Perley, R. A., Hjorth, J., et al. 2015, ApJ, 801, 102
Planck Collaboration, Ade, P. A. R., Aghanim, N., et al. 2014, A&A, 571, 16
Price, P. A., Berger, E., Reichart, D. E., et al. 2002, ApJL, 572, L51
Sari, R., Piran, T., & Narayan, R. 1998, ApJL, 497, L17
Savaglio, S., Glazebrook, K., & Le Borgne, D. 2009, ApJ, 691, 182
Shivvers, I., & Berger, E. 2011, ApJ, 734, 58
Soderberg, A. M., Kulkarni, S. R., Berger, E., et al. 2004, ApJ, 606, 994
Stanway, E. R., Bremer, M. N., Tanvir, N. R., et al. 2011, MNRAS, 410, 1496
Stanway, E. R., Davies, L. J. M., & Levan, A. J. 2010, MNRAS, 409, L74
Stanway, E. R., Levan, A. J., & Davies, L. J. M. 2014, MNRAS, 444, 2133
Thompson, A. R., Clark, B. G., Wade, C. M., & Napier, P. J. 1980, ApJS, 44, 151
Tingay, S. J., Goeke, R., Bowman, J. D., et al. 2013, PASA, 30, 7
van Haarlem, M. P., Wise, M. W., Gunst, A. W., et al. 2013, A&A, 556, 2
Wu, X. F., Dai, Z. G., Huang, Y. F., & Lu, T. 2005, ApJ, 619, 968
Wygoda, N., Waxman, E., & Frail, D. A. 2011, ApJL, 738, L23
Yüksel, H., Kistler, M. D., Beacom, J. F., et al. 2008, ApJL, 683, L5
Zhang, B., Fan, Y. Z., Dyks, J., et al. 2006, ApJ, 642, 354
Zhang, B., Kobayashi, S., & Mészáros, P. 2003, ApJ, 595, 950
Zhang, B., & Mészáros, P. 2004, IJMPA, 19, 2385
Zhang, B., Zhang, B. B., Virgili, F. J., et al. 2009, ApJ, 703, 1696
Zhang, Z. B., Kong, S. W., Huang, Y. F., et al. 2015, RAA, 15, 237